Surface and interface mediated magnetism in mesoscopic ceria@carbon core–shell structures

Duo Jia Lee [a], Pei-Kai Hsu [a], Yi-Che Chen [a], Alexandre Gloter [b,*], Shih-Yun Chen [a,*]

[a] Department of Materials Science and Engineering, National Taiwan University of Science and Technology, Taipei, Taiwan
[b] Laboratoire de Physique des Solides, CNRS, Université Paris-Saclay, 91405 Orsay, France

A B S T R A C T

CeO_2@C submicron core–shell structure was prepared by a two-step synthesis method, and the ceria shell thickness and its microstructure were precisely controlled by the precursor composition and annealing process. The results show that forming the thin ceria shell by aggregating nanoparticles on the surface of the carbon sphere is more favorable for forming ferromagnetism than merely dispersed ceria nanoparticles. The saturation magnetization increases with decreasing shell thickness, indicating the contributions of surfaces and interfaces to the magnetism. Furthermore, high-temperature reduction results in shell densification and the aggregation of defects at the surface. The spectroscopic and microscopic measurements reveal that in such cases, a continuous defect-rich area with a sub-nanometric thickness, doped with electrons extends over the whole surface of the mesostructure. The magnetic strength difference caused by adjusting the thickness of this defective layer from several nanometers to sub-nanometric width can reach 360 times, suggesting that the magnetization of these mesoscopic systems is related to the presence of these quasi-2D electron-rich regions on the surface. This study shows the applicability of giant orbital magnetism to mesoscopic systems, and the results can also provide a reference for the subsequent synthesis of magnetic materials.

1. Introduction

Spintronics is the combination of nanoscale electronics and magnetism, which aims to utilize the spin degree freedom of electrons for novel information storage and logic devices [1–4]. The information transmit speed is still high even derived by very low power. As a consequence, it becomes a possible solution to overcome the speed and energy consumption problems of traditional integrated circuits. Considering the component of these devices, spintronics with semiconductors is in particularly attractive as it can combine the potential of semiconductors with magnetic materials [5,6]. It could be built on hybrid structures associating ferromagnetic metals with nonmagnetic semiconductors or being based on the fabrication of ferromagnetic semiconductors [7–9]. In the latter one, ferromagnetism was introduced by doping with transition metals, which results in slight changes in the structure of the original material, and can greatly reduce the effects on other physical properties [10–13].

In addition to the transition metal doped semiconductors, different semiconducting oxides, including ZnO [14], TiO_2 [15], SnO_2 [16], CeO_2 [17], etc., have been reported to be ferromagnetic at room temperature even without doping. The ferromagnetic strength of these un-doped oxides was found to be closely related to the presence of defects [18–21]. Notably, oxide semiconductors are more likely to exhibit

ferromagnetism at the nanoscale due to size effects. However, when nanoparticles are composed of mesoscopic structures, such as films and spheres, the relationship between macroscopic magnetism and individual nanoparticles has not been elucidated. Up to now, only a few studies have clearly established the relationship between mesoscale structuration and magnetic generation. Esmaeily et al. have recently linked the presence of electrons associated with oxygen vacancies at the surfaces of the open pores created in an amorphous Al_2O_3 membrane with magnetism. The strength of the magnetism can be engineered by the controllable pore surface area or by coordinating ligands to surface aluminum ions [22]. Similarly, magnetism in $SrTiO_3$ substrate after various treatments and structuration (surface orientation, grinding to powders) have been compared and the magnetism has been associated with defects near the surface, or with the surface itself [23].

Various mechanisms have been proposed to explain the magnetic properties of un-doped oxide semiconductors [24–29]. Among them, the giant orbital paramagnetic model has attempted to provide an explanation for the magnetic generation mechanism of the mesoscopic systems constructed by nanoparticles. It is based on the presence of a microscopic coherent domain, due to the effect of zero-point radiation. The authors suggested that this mechanism is stable in 2D-like structures with a large surface-volume ratio [24,25]. The stabilization of the coherent domain indeed implies a very thin layer, ideally of atomic size

* Corresponding authors.
E-mail addresses: gloter@universite-paris-saclay.fr (A. Gloter), sychen@mail.ntust.edu.tw (S.-Y. Chen).

with an high density of defects. No cavity is required in the model but the size of the coherent domains is determined by wavelengths corresponding to electronic excitations associated to the materials. In the case of the CeO_2 nanoparticles, it has been associated to the ultraviolet absorption spectrum and a characteristic length scale of order 100 nm for the magnetism to appear in CeO_2 nanoparticle clusters has been proposed. Several parameters such as the numbers of surface atoms and of defects or the excitation energy and the dielectric constant have been discussed for the occurrence of such magnetism [24,25]. Ceria has been suggested as a possible case, with an expected strong dependency to the experimentally controlled defective shell thicknesses since the model privilege a thickness of the surface layer with atomic dimensions.

Therefore, the synthesis and study of mesoscopic oxide spheres with different surface properties will help clarify the above-mentioned mechanism, and facilitate the subsequent regulation of properties, which can improve its applicability in the fields of energy, medicine, and environment [30,31].

In this study, we investigate the magnetic properties of a ceria (CeO_2) shell deposited on top of a submicron-sized carbon sphere by a template method. The carbon sphere has radii of several hundreds of nanometers that is above the minimum size for a coherent domain and would typically match the strong UV absorption of ceria. The thickness, surface roughness, compactness, and continuity of the ceria shell were then regulated by varying the precursor composition and the post-reduction treatments. Spectroscopic and microscopic measurements were performed to investigate the evolution of the defect distribution, especially their spatial extension at the surface, interface, and within the shell. Then the correlation between the structure of mesoscopic materials and their magnetic properties was explored and compared with related models.

2. Experimental procedures

2.1. Synthesis of carbon spheres

Carbon spheres were prepared by a hydrothermal method. First, glucose ($C_6H_{12}O_6$, 99.5%, Vetec) was added to deionized water and stirred at 500 rpm for five minutes to dissolve uniformly. The solution was then transferred to a stainless-steel autoclave and heated at 200 °C for 3.5 h. The mixture was then washed with deionized water and ethanol by centrifugation at 6000 rpm to obtain the precipitate. Finally, carbon spheres can be obtained after drying at 80 °C for 24 h.

2.2. Synthesis of CeO_2@C core–shell structure

The deposition of CeO_2 nanoparticles on carbon spheres was carried out by a sol-gel method. Cerium (III) nitrate hexahydrate (Ce $(NO_3)_3 \bullet 6H_2O$, 99.5%, Alfa Aesar) and carbon spheres were placed in deionized water. The molar ratios of Ce $(NO_3)_3$ to C spheres were set as 1:16, 1:14, and 1:10, and the samples were named T1, T2, and T3. In addition, the deposition was repeated twice at a ratio of 1:12 and named T4. Ammonium hydroxide (NH_4OH, NH_3 content 28%, J. T. Baker) was then added dropwise until the pH value reached 10. The precipitates were collected by centrifugation and washed with deionized water and ethanol. The precipitate was then dispersed in a 0.1 M solution of urea (CH_4N_2O, J. T. Baker). The pH of the solution was adjusted by the dropwise addition of hydrochloric acid (HCl, 36.5~38%, J. T. Baker) solution to a pH of 2 and stirred for 30 min. The mixture was washed with deionized water and ethanol and dried under 80 °C for 24 h to get the CeO_2@C core–shell structure.

2.3. Characterization

The crystal structures were characterized by X-ray Diffractometer (XRD) with Cu K radiation (Bruker D2 PHASER XE-T XRD) and Raman scattering spectrometer (HORIBA iHR550) with an excitation wavelength of 532 nm. The surface topography was studied by atomic force microscopy (Bruker Dimension ICON). The microstructures were investigated using transmission electron microscope (FEI Tecnai™ G2 F-20 S-TWIN). The STEM-EELS analysis was done with a Nion STEM microscope operated at 100 keV. EELS valence quantification was done by fitting the Ce–M edges with reference spectra (fluorite CeO_2 and CeF_2 for Ce^{4+}/Ce^{3+}). X-ray absorption measurements were carried out at National Synchrotron Radiation Research Center (NSRRC) in Taiwan. The X-ray absorption near edge fine structures (XANES) spectra at the Ce L_3-edge was performed at a DCM tender X-ray beamline 16A with energy resolution set to 0.25 eV. The magnetic properties were measured using a vibrating sample magnetometer (VSM) at room temperature at the Institute of Physics, Academia Sinica, Taiwan.

3. Results and discussion

The crystal structure was first determined by XRD. All samples are confirmed to be ceria with a face-centered cubic fluorite structure as compared to the JCPD database (43-1002), and no other crystallite phase was detected (Fig. S1).

The TEM images of samples T1 to T4 are demonstrated in Fig. 1 (a–d). As the concentration of Ce in the precursor increases, more particles are deposited on the carbon spheres. It is worth noting that the distribution of the particles is not uniform showing an increasing roughness from samples T1 to T4. The cross-sectional TEM and STEM-HAADF observations for sample T1 are present in Fig. 1(e) and (f), respectively. A clear core-shell structure can be seen. The shell is uniform with a thickness average of about 6 nm, most of the shell's width is between 4 and 10 nm. The high-resolution STEM-BF observation demonstrates that the shell is typically composed of only one to three particles, usually well attached (Fig. 1(g)).

In contrast, cross-sectional STEM observations (Fig. 1(h) and (i)) of sample T3 reveal a strong inhomogeneity of the shell. Variations of thickness among regions could be larger than 50 nm. The high-resolution TEM image of sample T3 confirms that the shell is always thick (Fig. 1(j)), but its density becomes lower after several nanometers away from the carbon sphere. The crystallinity of these particles is high, of which the lattice fringes are visible and can correspond to the (111) plane of CeO_2.

The deposition of nanoparticles with different concentrations of Ce on carbon spheres was investigated by AFM (Fig. 2). It demonstrates that as the concentration of Ce in the precursor increases, a thin network structure is formed on the carbon sphere first (T1). Then large-scale islands and an increased roughness are observed (T3). Such results are consistent with TEM observations.

To manipulate the internal structure of the shell, sample T3 was annealed in a reducing atmosphere (Ar + 3% H_2) at 300 °C and 500 °C for two hours. The obtained samples were named T3-R1 and T3-R2, respectively. The XRD results confirmed that all nanoparticles are ceria FCC fluorite structure and the crystallinity is improved (Fig. S2). The high-resolution cross-sectional TEM images of the two samples show that the shell becomes dense. The shell thickness of samples T3-R1 and T3-R2 decreased to 6.9 nm and 8.5 nm, respectively (Fig. S3), starting from an estimated shell thickness of *ca.* 10 nm for sample T3. The decrease of shell thickness can be attributed to the increase of shell density during sintering process. The surface morphology of the reduced samples observed by AFM (Fig. S4) shows a very different surface topography from sample T3. The large-scale island-like structure transformed into a smooth and continuous layer.

Fig. 3 demonstrates the Raman spectrum of samples T1 to T4. In the Raman shift range between 350 and 650 cm^{-1} (Fig. 3(a)), there is only one band, F_{2g} locates at 464 cm^{-1}, which is assigned to the symmetric stretching vibration mode of Ce and O atoms [32]. It is found that the band of sample T1 locates at a high wavenumber and exhibits a small full width at half maximum. With the increase of the Ce content in the precursor, the band shifts to the lower wavenumber side, and the
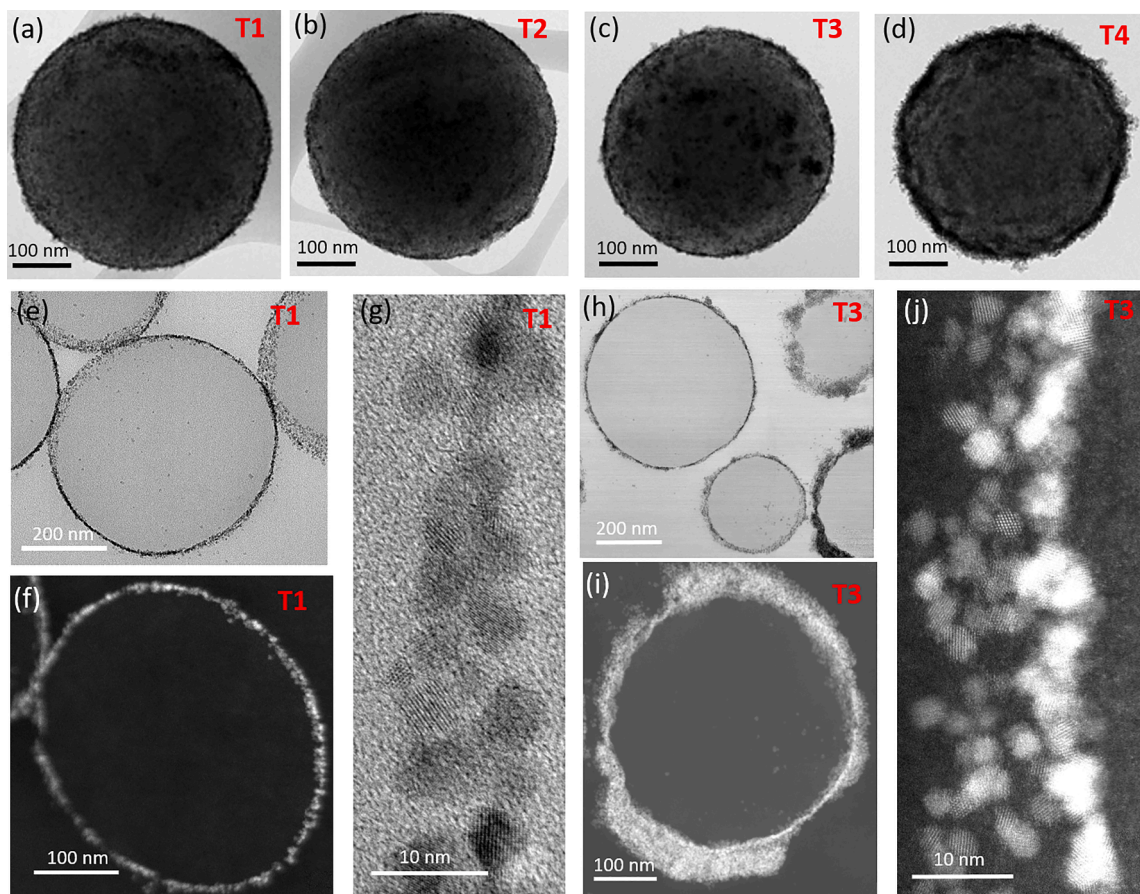
Fig. 1. (a-d) TEM images of samples T1 to T4. (e) The cross-sectional TEM, (f) cross-sectional STEM-HAADF observations, and (g) high-resolution STEM-BF observation for sample T1. (h) The cross-sectional TEM, (f) cross-sectional STEM-HAADF observations, and (g) high resolution STEM-HAADF observation for sample T3.
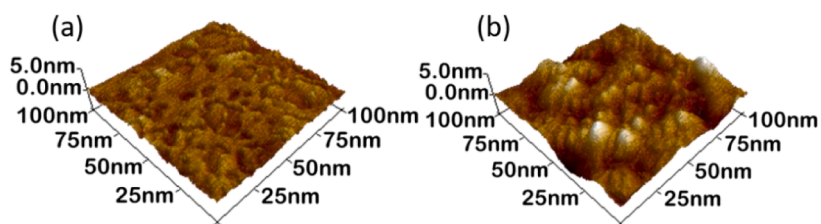
Fig. 2. AFM observations of (a) sample T1 and (b) T3.

bandwidth increases. The relationship between the shell thickness and the change in the F_{2g} band is plotted in the insert figure, implying that the defects in the ceria increase with the increment of the shell thickness [33]. It is in accordance with the microscopic observation that indicated less dense and thus more surface-exposed particles when the shell gets thicker.

On the other hand, Fig. 3(b) shows the two characteristic vibration bands of carbon, which are the D-band locates between 1320 cm^{-1} and 1360 cm^{-1} and the G-band locates between 1500 cm^{-1} and 1600 cm^{-1}. The former is caused by the breathing mode of the sp[2] atoms in the ring structure while the latter results from the bond stretching of pairs of sp[2] atoms in cyclic and chain structures [34]. In general, the D-band represents the presence of disordered graphitic structures, and the G-band represents the presence of ordered graphitic structures [35]. It is

found that the spectrum of all samples is similar to the bare carbon spheres (T0). The I_D/I_G values of T1 to T4 are 0.46, 0.41, 0.40, and 0.44, respectively, indicating that the carbon in all samples is amorphous [36]. In the reduced sample, the peak of F_{2g} shifts to a lower wavenumber, and the half-width increases, confirming the increase of defects after reduction (Fig. S5 (a)). On the other hand, no difference was observed among these samples in both the positions and relative intensities of the D-band and G-band (Fig. S5 (b)).

The electronic structures were investigated by XAS. XANES of the Ce L_3-edge of each sample is shown in Fig. S6 (a). Ce L_3-edge contains five peaks, of which A_1 and A_2 are the final energy states of $2p^4f^05d*$ of Ce^{4+}. B is the final energy state of $2p^4f^15d*\underline{L}$ of Ce^{4+}. D is contributed by dipole forbidden transition. Component C is produced by Ce^{3+}. The content of Ce^{3+} can be obtained by calculating the proportion of the area
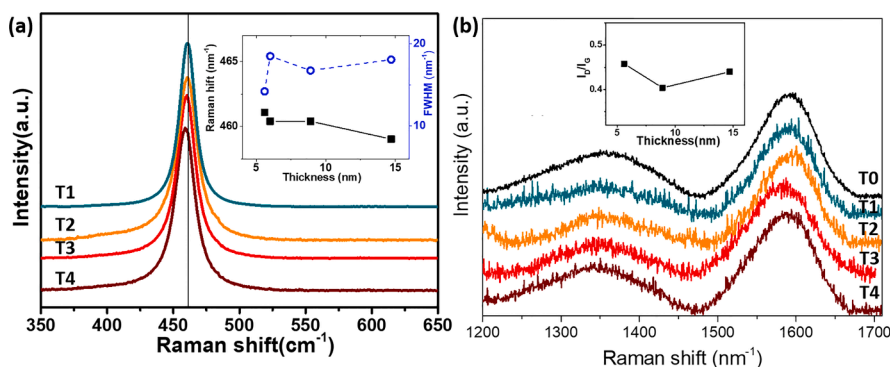
Fig. 3. Raman spectrum of samples T1 to T4. (a) F_{2g} band of the ceria shell. The changes in Raman shift and FWHM of the band with increasing the shell thickness were plotted in the insert figure. (b) D band and G band of the carbon sphere. The ratio between these two bands of samples with different shell thickness was shown in the insert figure.

of component C in the entire *L*-edge [37]. The estimated Ce^{3+} content of sample T1 to T4 are 13.3%, 17%, 10.6% and 12.2%, respectively. No strong correlation between shell thickness and the Ce^{3+} content is found. On the other hand, the Ce^{3+} content of samples T3-R1 and T3-R2 was found to be 16.0% and 10.5%, respectively (Fig. S6 (b)). The less increase of Ce^{3+} content of sample T3-R2 can be attributed to the competitive effect between reduction and grain growth at high temperatures.

The magnetic behavior of the samples was measured by VSM at room temperature. Fig. S7 (a) shows the magnetic contribution from sample holder. Fig. S7 (b) shows the M-H curves of samples T1 to T4 after the deduction of the contribution from sample holder. Different magnetic behaviors were detected together. The diamagnetic contribution can be estimated by the slope of the curve at high magnetic fields. The ferromagnetic behavior of samples T1 to T4 after deducting the above background contribution are shown in Fig. 4(a). The coercivity, Hc, of sample T1 is 70 Oe, which is close to that of the bare carbon sphere (T0). For the other three samples, Hc is enhanced up to 200 Oe. Such values are close to the results in the literature [38–40]. The coercive magnetic field of the annealed or surface-treated CeO_2 nanoparticles and their core-shell structure is between 80 and 400 Oe. The saturation magnetization of the bare carbon spheres is 0.0011 emu/g. After deducting the magnetic contribution of carbon spheres, the saturation magnetization of the ceria (Ms-CeO_2) of each sample can be obtained. The Ms-CeO_2 was 0.036 emu/g, 0.008 emu/g, 0.007 emu/g, and 0.012 emu/g of samples T1, T2, T3, and T4, respectively. All the values are higher than those of micrometer-scaled CeO_2 hollow spheres with various surface treatments [38–40].

The M-H curves of the samples obtained after reducing the T3 are plotted in Fig. 4(b). All samples exhibit ferromagnetic properties and the Hc drop to 50 and 70 Oe of samples T3-R1 and T3-R2, respectively. Notably, the magnetization was enhanced significantly after reduction, in particular the sample T3-R2. After deducting the contribution of

carbon spheres, the saturation magnetization of the CeO_2 shells (Ms-CeO_2) in samples T3-R1 and T3-R2 are 0.07 emu/g and 0.22 emu/g, respectively. The latter one is close to the highest value in the literature related to the CeO_2 system [40–42].

STEM-EELS experiments were then conducted to investigate the local cerium valence distribution. Fig. 5(a) gives an example for the sample T3-R2 where the STEM-HAADF image measured online during the spectro-microscopy measurement can be seen at the top left. Every spectrum from the spectral data cube has been fitted by the Ce–M edge for Ce^{4+} and Ce^{3+} reference compounds visible in Fig. 5(b). The fitting weight for the Ce^{3+} and Ce^{4+} components, and the resulting $Ce^{3+}/\Sigma Ce$ maps are in shown Fig 5(a) and evidence for that sample a very narrow Ce^{3+} enriched lines at the surface of the nano-particles that will be discussed later. Fig. 5(c) shows the spectra from that surface line, and the bulk of this last nanoparticle. A strong evolution of the cerium valence is observed over solely 2 nm from the surface to the central part of the particle with a ratio evolution from ca. 80/20 to ca. 20/80 for the $Ce^{3+}/\Sigma Ce$ ratio.

Fig. 6 compares the STEM-HAADF and EELS-based Ce^{3+} quantification typical of sample T1, T3, and T3-R2 ceria shells. In addition, threshold images where the pixels with $Ce^{3+}/\Sigma Ce$ intensity above 0.6 have been set to 1 (and to zero for values below that threshold) are presented. It highlights the Ce^{3+} rich areas in the scope of discussing their size extensions and connectivity.

As demonstrated in Fig. 6(a), sample T1 has a shell typically composed of 1 to 3 nanoparticles widths that are densely packed. There is a Ce^{3+}-enriched region with a thickness of about 2 nm that extends to the surface of the last particle, showing quite good continuity. Sample T3 has often a thicker shell that shows weak compaction. Due to the limited field of view for EELS spectrum imaging, Fig. 6(b) is an example with a rather small ceria shell, but where porosities are present (marked by the yellow ovals). The overall Ce^{3+} content is higher, notably for the particles at the surface, id est, located beyond the porosity line. This is
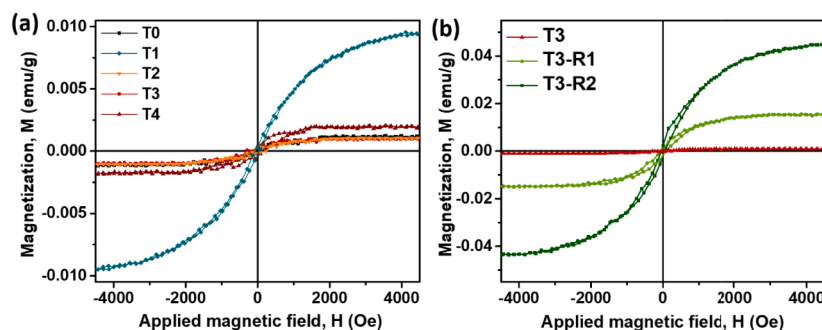
Fig. 4. (a) M-H curves obtained at room temperature of samples T0 to T4. (b) M-H curves of sample T3 and T3 with different reduction treatments.
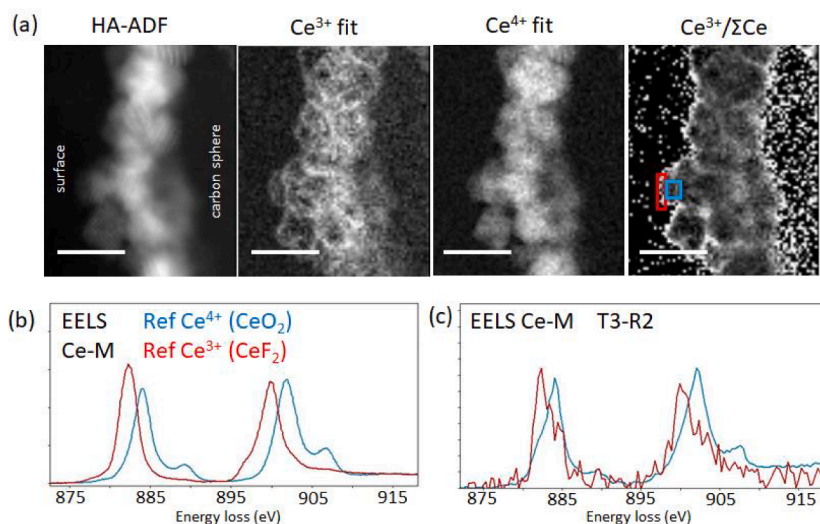
Fig 5. (a) HAADF-STEM, Ce^{3+}, Ce^{4+} and $Ce^{3+}/\Sigma Ce$ maps measured by STEM-EELS experiment for the T3-R2 sample, (b) reference EELS spectra used for a quantification of the Ce^{3+} and Ce^{4+} contribution, (c) typical EELS Ce-M spectra at the surface of the last particle and at the central part of the last particle (at ca. 2 nm from the surface). The positions of the spectra are indicated by colored boxes in the $Ce^{3+}/\Sigma Ce$ map of (a). All scale bars are 10 nm long.
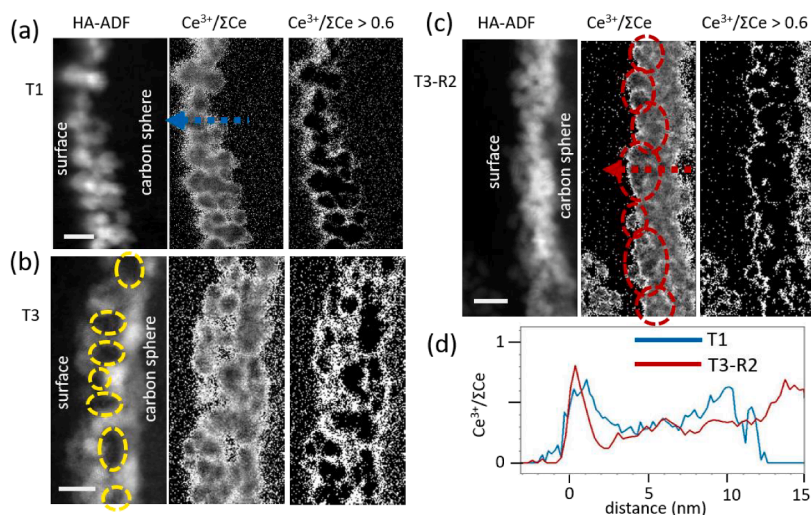
Fig. 6. HAADF-STEM, $Ce^{3+}/\Sigma Ce$ maps, and thresholded maps above $Ce^{3+}/\Sigma Ce = 0.6$ for (a) T1, (b) T3 and, (c) T3-R2. The yellow ovals in HAADF-STEM image of (b) indicate the pores within the ceria shell of T3. The red ovals in the Ce^{3+} maps of (c) indicate the surface nanoparticles with a darker contrast indicating Ce^{3+} depleted areas. (d) Typical profiles of the $Ce^{3+}/\Sigma Ce$ content near the surface (corresponding to the distance = 0 nm) of the nanoparticles for T1 and T3-R2. At the surface of T1, the Ce^{3+} gaz extend over ca. 2 nm while it is limited to < 1 nm for T3-R2 due to the migration of the oxygen vacancies to the surface. For both samples, the Ce^{3+} extension at the interface with the carbon sphere (located at a distance of ca. 10 and ca. 15 nm for respectively T1 and T3-R2) is of ca. 2 nm. The areas for the profiles are indicated by arrows in the images (a) and (c). All scale bars are 10 nm long.

rather normal since they have many exposed surfaces. The Ce^{3+}-rich regions are then rather wider than that of sample T1, with more complicated connectivity due to the pores. After reduction, the ceria layer becomes thinner and denser (sample T3-R2, Fig. 6(c)). Notably, the last particles have very low Ce^{3+} at the inner part, as evidenced by the darker areas in the $Ce^{3+}/\Sigma Ce$ images (marked by red ovals). On the other hand, their surfaces show very thin Ce^{3+} enriched lines that propagate over the whole surface with good connectivity between particles. The spectra in Fig. 6(c) were typically from the narrow Ce^{3+}-rich line and the low Ce^{3+} bearing inner part for the last particles of sample T3-R2. The profiles of the Ce^{3+} distribution typical for samples T1 and T3-R2 are compared in Fig. 6(d), showing that the Ce^{3+} surface area is typically 2 nm for the sample T1 but is reduced to a sub-nanometric width for the sample T3-R2.

Combining the above spectral and microscopic analysis results, the reasons for the differences in magnetic strength between samples with different shell structures can be explored. The first possibility is the increase of the surface and interface area caused by the thinning of the

CeO₂ shell. According to TEM observations, when the shell thickness decreased from 15 nm (sample T4) to 5 nm (sample T1), the surface area of CeO₂ shell and the interface area between CeO₂ and carbon spheres increased by about 24% and 46%, respectively. However, the ferromagnetic strength increases by as much as 200%. Such results indicate that the magnetic enhancement is not simply related to the surface and interfacial area of the ceria shell. The second possible reason is the additional contribution caused by interfacial reactions, as seen in Ag@CeO₂ core-shell structure composites [43]. However, in this study, no significant interaction between CeO₂ particles and carbon spheres was observed, either by spectroscopic or microscopic studies.

The effect of defects on the magnetic formation process is then considered. Among the shell-structured ceria samples without annealing, the microscopic investigation evidences a Ce^{3+}-rich layer of ca. 2 nm in width at the interface and surface with connectivity that depends on the shell structure, in particular of the shell surface roughness. On that aspect, the comparison between samples T1 and T3 is enlightening. Sample T1 possesses a lower thickness, a smaller surface roughness, and

a higher defect concentration than sample T3, and its magnetic strength is 60 times higher. Such difference cannot be explained by a dilution effect due to the shell thickness as described above. The main difference resides in the nature of the defective layer near the surface. While sample T1 has a rather continuous thin defective layer that can be seen as a quasi-2D system, sample T3 has much more complex defect networks due to the pores, with several Ce^{3+} percolation paths and, as a result, a much extended area with an overall higher Ce^{3+} content near the surface.

It is even more striking to compare sample T3 with T3-R2. Notably, the difference in shell thickness is small between these two samples. The main difference is in the surface topography and the Ce^{3+} distribution. Indeed, a smooth surface with an extremely narrow Ce^{3+}-rich layer is obtained after reduction. As a result, a magnetic reinforcement as high as 360 times is retrieved. It demonstrates that the continuity and width of these defective quasi-2D layers located on the shell surface are important parameters affecting the magnetic strength. For that sample, the Ms of 0.22 emu.g^{-1} can be converted to *ca.* 1 μ_B per nm^2 assuming that the magnetism is derived by the surface. Such value is in the same order as reported for the surface magnetism of $SrTiO_3$ substrate [23]. Such a hypothesis can be further supported by comparing sample T1 with T3-R2. Both samples have similar surface roughness and defects content, the main difference is the reduced width of the defective quasi-2D layer. Notably, the Ms of sample T3-R2 is 6 times higher than that of sample T1.

At last, the influence of structural changes at the mesoscopic scale on the magnetic properties is discussed. In order to demonstrate the effect of structural changes at the mesoscopic scale, the Ms values of these ceria shells were compared with those of bare CeO_2 nanoparticles using the same synthesis process but without carbon spheres. The obtained nanoparticles were named as sample NP. Then the particles were annealed at 500 °C for 2 h under reducing atmosphere, and named as sample NP-R2. The M–H curves of these two samples are shown in Fig. S8. The Hc of sample NP is 200 Oe and the Ms is 0.0008 emu/g. Compared with the samples composed of spherical shell structure (samples T1-T4), the magnetization is lower by more than one order of magnitude. On the other hand, the Hc of sample NP-R2 is 100 Oe and the Ms is 0.0006 emu/g. Compared with the spherical shell structure sample after the same reduction treatment process (sample T3-R2), its magnetization is lower by more than two orders of magnitude. The above results suggest that changes in the mesoscale structure, i.e., whether the particles are in a dispersed state or aggregated into spherical shells, have an important impact on the overall magnetic generation mechanism. Such results are consistent with previous reports. [26] Disruption of CeO_2 aggregate has already been reported to strongly weaken the magnetism and an inferior limit of *ca.* 100 nm was deduced for preserving the magnetic properties.

As a consequence, our study demonstrated that forming a shell by aggregating ceria particles over a submicronic sphere is beneficial for magnetic strength. Furthermore, the Ms of the shell strongly depends on the surface of the shell and notably the width and continuity of the quasi-2D defective areas showing a high electron doping. Such a dependence might be explained by a magnetism occurring via the formation of a giant orbital moment associated with coherent orbital currents over the shell. Similar core-shell structures have been synthesized in recent years, but the emphasis is on the improvement of redox ability and mechanical strength to promote applications in catalysis and grinding [44–46]. This study also pointed out that this structure is ferromagnetic, and its strength can be further adjusted through a simple process and could further expand its applicability.

4. Conclusions

$CeO_2@C$ submicron core–shell structure was prepared by a two-step synthesis method, and the ceria shell thickness and its microstructure were precisely controlled. It revealed that forming the thin spherical ceria shell by aggregating nanoparticles on the surface of the carbon sphere is more favorable for forming ferromagnetism than merely dispersed nanoparticles. The shell thickness-dependent magnetization indicates the contributions of surfaces and interfaces to the magnetism. Furthermore, after high-temperature reduction, a continuous defect-rich area with a sub-nanometric thickness, doped with electrons extends over the whole surface of the mesostructure. Magnetic strength could be varied over 360 times by adjusting the thickness of this defective layer from several nanometers to sub-nanometric width. Such a dependence might be explained by a magnetism occurring via the formation of a giant orbital moment associated with coherent orbital currents over the shell.

Credit authorship contribution statement

Duo Jia Lee: Formal analysis, Validation, Writing.
Pei-Kai Hsu: Formal analysis, Validation.
Yi-Che Chen: Formal analysis, Validation.
Alexandre Gloter: Methodology, Resources, Formal analysis, Writing -review & editing.
Shih-Yun Chen: Investigation, Conceptualization, Formal analysis, Writing - original draft, Writing - review &editing, Supervision, Project administration, Funding acquisition

Declaration of Competing Interest

The authors declare that they have no known competing financial interests or personal relationships that could have appeared to influence the work reported in this paper.

Data availability

No data was used for the research described in the article.

Acknowledgment

References

[1] S.A. Wolf, D.D. Awschalom, R.A. Buhrman, J.M. Daughton, S.V. Molnar, M. L. Roukes, A.Y. Chtchelkanova, D.M. Treger, Spintronics: a spin-based electronics vision for the future, Science 294 (2001) 1488–1495.

[2] I. Zutic, J. Fabian, S.D. Sarma, Spintronics: fundamentals and applications, Rev. Mod. Phys. 76 (2004) 323–410.

[3] A. Fert, Nobel lecture: origin, development, and future of spintronics, Rev. Mod. Phys. 80 (2008) 1517–1530.

[4] S.D. Bader, S.S.P. Parkin, Spintronics, Annu. Rev. Condens. Matter Phys. 1 (2010) 71–88.

[5] N. Samarth, S.H. Chun1, K.C. Ku, S.J. Potashnik, P. Schiffer, Hybrid ferromagnetic/ semiconductor heterostructures for spintronics, Solid State Commun. 127 (2003) 173–179.

[6] D.D. Awschalom, M.E. Flatté, Challenges for semiconductor spintronics, Nat. Phys. 3 (2007) 153–159.

[7] E.I. Rashba, Theory of electrical spin injection: tunnel contacts as a solution of the conductivity mismatch problem, Phys. Rev., B 62 (2000) R16267–R16270.

[8] H. Ohno, A. Shen, F. Matsukura, A. Oiwa, A. Endo, S. Katsumoto, Y. Iye, (Ga,Mn) As: a new diluted magnetic semiconductor based on GaAs, Appl. Phys. Lett. 69 (1996) 363–365.

[9] H. Ohno, Ferromagnetic semiconductors for spintronics, Physica B 19 (2006) 376–377.

[10] J.B. Cui, Q. Zeng, U.J. Gibson, Synthesis and magnetic properties of Co-doped ZnO nanowires, J. Appl. Phys. 99 (2006) 08M113.

[11] Y. Ding, W.Q. Han, L.H. Lewis, Enhanced magnetism in Fe-doped TiO_2 anatase nanorods, J. Appl. Phys. 102 (2007), 123902.

[12] G. Shihui, Y. Jinglei, Z. Huaxin, Magnetic properties of diluted magnetic semiconductor nanowires $Co_xSn_{1-x}O_2$, J. Appl. Phys. 104 (2008), 063906.

[13] K. Srinivas, S.M. Rao, P.V. Reddy, Structural, electronic and magnetic properties of $Sn_{0.95}Ni0.05O_2$ nanorods, Nanoscale 3 (2011) 642–653.

[14] B. Qi, S. Ólafsson, H.P. Gíslason, Vacancy defect-induced d° ferromagnetism in undoped ZnO nanostructures: controversial origin and challenges, Prog. Mater. Sci. 90 (2017) 45–74.

[15] B. Santara, P.K. Giri, S. Dhara, K. Imakita, M. Fujii, Oxygen vacancy-mediated enhanced ferromagnetism in undoped and Fe-doped TiO_2 nanoribbons, J. Phys. D: Appl. Phys. 47 (2014), 235304.

[16] V.B. Kamble, S.V. Bhat, A.M. Umarji, Investigating thermal stability of structural defects and its effect on d° ferromagnetism in undoped SnO_2, J. Appl. Phys. 113 (2013), 244307.

[17] S.Y. Chen, Y.H. Lu, T.W. Huang, D.C. Yan, C.L. Dong, Oxygen vacancy dependent magnetism of CeO_2 nanoparticles prepared by thermal decomposition method, J. Phys. Chem. C 114 (2010) 19576–19581.

[18] V.R. Akshay, B. Arun, S. Dash, A.K. Patra, G. Mandal, G.R. Mutta, A. Chanda, M. Vasundhara, Defect mediated mechanism in undoped, Cu and Zn-doped TiO_2 nanocrystals for tailoring the band gap and magnetic properties, RSC Adv. 8 (2018) 41994–42008.

[19] B. Santara, P.K. Giri, K. Imakitab, M. Fujii, Evidence of oxygen vacancy induced room temperature ferromagnetism in solvothermally synthesized undoped TiO_2 nanoribbons, Nanoscale 5 (2013) 5476–5488.

[20] N.H. Hong, J. Sakai, N. Poirot, V. Brizé, Room-temperature ferromagnetism observed in undoped semiconducting and insulating oxide thin films, Phys. Rev., B 73 (2006), 132404.

[21] S. Ning, P. Zhan, Q. Xie, W. Wang, Z. Zhang, Defects-driven ferromagnetism in undoped dilute magnetic oxides: a review, J. Mater. Sci. Technol. 31 (2015) 969–978.

[22] A.S. Esmaeily, M. Venkatesan, S. Sen, J.M.D. Coey, D-zero magnetism in nanoporous amorphous alumina membranes, Phys. Rev. Mater. 2 (2018), 054405.

[23] J.M.D. Coey, M. Venkatesan, P.J. Stamenov, Surface magnetism of strontium titanate, Phys.: Condens. Matter 28 (2016), 485001.

[24] M. Coey, K. Ackland, M. Venkatesan, S.C. Sen, Collective magnetic response of CeO_2 nanoparticles, Nat. Phys. 12 (2016) 694–699.

[25] S. Sen, K.S. Gupta, J.M.D. Coey, Mesoscopic structure formation in condensed matter due to vacuum fluctuations, Phys. Rev., B 92 (2015), 155115.

[26] G. Bouzerar, T. Ziman, Model for vacancy-induced d° ferromagnetism in oxide compounds, Phys. Rev. Lett. 96 (2006), 207602.

[27] X. Han, J. Lee, H.I. Yoo, Oxygen-vacancy-induced ferromagnetism in CeO2 from first principles, Phys. Rev. B 79 (2009), 100403(R).

[28] J.M.D. Coey, M. Venkatesan, C.B. Fitzgerald, Donor impurity band exchange in dilute ferromagnetic oxides, Nat. Mater. 4 (2005) 173–179.

[29] L.R. Shah, B. Ali, H. Zhu, W.G. Wang, Y.Q. Song, H.W. Zhang, S.I. Shah, J.Q. Xiao, Detailed study on the role of oxygen vacancies in structural, magnetic and transport behavior of magnetic insulator: Co–CeO_2, J. Phys.: Condens. Matter 21 (2009), 486004.

[30] Y.F. Zhu, D.H. Fan, W.Z. Shen, A general chemical conversion route to synthesize various ZnO-based core/shell structures, J. Phys. Chem. C 112 (2008) 10402–10406.

[31] Y. Liu, Y. Chu, Y. Zhuo, L. Dong, L. Li, M. Li, Controlled synthesis of various hollow Cu nano/microstructures via a novel reduction route, Adv. Funct. Mater. 17 (2007) 933–938.

[32] W.J. Hong, S. Iwamoto, S. Hosokawa, K. Wada, H. Kanai, M. Inoue, Effect of Mn content on physical properties of CeO_x–MnO_y support and BaO–CeO_x–MnO_y catalysts for direct NO decomposition, J. Catal. 277 (2011) 208–216.

[33] S. Gnanam, V. Rajendran, Influence of various surfactants on size, morphology, and optical properties of CeO_2 nanostructures via facile hydrothermal route, J. Nanopart. (2013), 839391.

[34] A. Dychalska, P. Popielarski, W. Frankow, K. Fabisiak, K. Paprocki, M. Szybowicz, Study of CVD diamond layers with amorphous carbon admixture by raman scattering spectroscopy, Mater. Sci.-Pol 33 (2015) 799–805.

[35] A.C. Ferrari, J. Robertson, Raman spectroscopy of amorphous, nanostructured, diamond–like carbon, and nanodiamond, Philos. Trans. R. Soc. Lond. A 362 (2004) 2477–2512.

[36] A.S. Saleemi, R. Singh, Z. Luo, X. Zhang, Structure dependent negative magnetoresistance of amorphous carbon thin films, Diam. Relat. Mater. 72 (2017) 108–113.

[37] P. Nachimuthu, W.C. Shih, R.S. Liu, L.Y. Jang, J.M. Chen, The study of nanocrystalline cerium oxide by x-ray absorption spectroscopy, J. Solid State Chem. 149 (2000) 408–413.

[38] E.N. Tseng, Y.T. Hsiao, Y.C. Chen, S.Y. Chen, A. Gloter, J.M. Song, Magnetism and plasmonic performance of mesoscopic hollow ceria spheres decorated with silver nanoparticles, Nanoscale 11 (2019) 3574–3582.

[39] P.K. Hsu, Y.C. Chen, A. Gloter, H.C. Chen, E.N. Tseng, S.Y. Chen, J.M. Song, Surface-sensitive magnetism of mesoscopic hollow CeO_2 spheres, Mater. Sci. Eng., B 274 (2021), 115481.

[40] H.C. Chien, B.Y. Wu, P.K. Hsu, Y.C. Chen, J.M. Song, A. Gloter, S.Y. Chen, Tunable fluorescence and magnetic properties of ceria- organic core- shell hollow structures, Appl. Surf. Sci. 597 (2022), 153685.

[41] S.Y. Chen, C.H. Tsai, M.Z. Huang, D.C. Yan, T.W. Huang, A. Gloter, C.L. Chen, H. J. Lin, C.T. Chen, C.L. Dong, Concentration dependence of oxygen vacancy on the magnetism of CeO_2 nanoparticles, J. Phys. Chem. C 116 (2012) 8707–8713.

[42] K. Ackland, J.M.D. Coey, Room temperature magnetism in CeO_2—a review, Phys. Rep. 746 (2018) 1–39.

[43] S.Y. Chen, E. Tseng, Y.T. Lai, W. Lee, A. Gloter, Interface interactions and enhanced room temperature ferromagnetism of Ag@CeO_2 nanostructures, Nanoscale 9 (2017) 10764–10772.

[44] T. Wang, Y. Chen, A. Chen, Y. Chen, Development of carbon sphere/ceria (CS/CeO_2) heterostructured particles and their applications to functional abrasives toward photochemical mechanical polishing, Appl. Surf. Sci. 593 (2022), 153449.

[45] W. Wu, W. Qi, Y. Zhao, X. Tang, Y. Qiu, D. Su, H. Fan, G. Wang, Hollow CeO_2 spheres conformally coated with graphitic carbon for high performance supercapacitor electrodes, Appl. Surf. Sci. 463 (2019) 244–252.

[46] N. Wang, W. Li, Y. Ren, J. Duan, X. Zhai, F. Guan, L. Wang, B. Hou, Investigating the properties of nano core-shell CeO_2@C as haloperoxidase mimicry catalyst for antifouling applications, Colloids Surf. A 608 (2021), 125592.